agriculture

MDPI

Article

Analysis and Experimentation on the Motion Characteristics of a Dragon Fruit Picking Robot Manipulator

Kairan Lou [1], Zongbin Wang [1], Bin Zhang [1,2], Qiu Xu [1], Wei Fu [1,2,*], Yang Gu [2] and Jinyi Liu [1]

[1] Mechanical and Electrical Engineering College, Hainan University, Haikou 570228, China; 22210828010001@hainanu.edu.cn (K.L.); 22220854060028@hainanu.edu.cn (Z.W.); 21110810000031@hainanu.edu.cn (B.Z.); 23220855000012@hainanu.edu.cn (Q.X.); 993632@hainanu.edu.cn (J.L.)

[2] School of Information and Communication Engineering, Hainan University, Haikou 570228, China; guyangl@hainanu.edu.cn

* Correspondence: 994026@hainanu.edu.cn

Abstract: Due to the complex growth positions of dragon fruit and the difficulty in robotic picking, this paper proposes a six degrees of freedom dragon fruit picking robot and investigates the manipulator's motion characteristics to address the adaptive motion issues of the picking manipulator. Based on the agronomic characteristics of dragon fruit cultivation, the structural design of the robot and the dimensions of its manipulator were determined. A kinematic model of the dragon fruit picking robot based on screw theory was established, and the workspace of the manipulator was analyzed using the Monte Carlo method. Furthermore, a dynamic model of the manipulator based on the Kane equation was constructed. Performance experiments under trajectory and non-trajectory planning showed that trajectory planning significantly reduced power consumption and peak torque. Specifically, Joint 3's power consumption decreased by 62.28%, and during the picking, placing, and resetting stages, the peak torque of Joint 4 under trajectory planning was 10.14 N·m, 12.57 N·m, and 16.85 N·m, respectively, compared to 12.31 N·m, 15.69 N·m, and 22.13 N·m under non-trajectory planning. This indicated that the manipulator operates with less impact and smoother motion under trajectory planning. Comparing the dynamic model simulation and actual testing, the maximum absolute error in the joint torques was −2.76 N·m, verifying the correctness of the dynamic equations. Through field picking experiments, it was verified that the machine's picking success rate was 66.25%, with an average picking time of 42.4 s per dragon fruit. The manipulator operated smoothly during each picking process. In the study, the dragon fruit picking manipulator exhibited good stability, providing the theoretical foundation and technical support for intelligent dragon fruit picking.

Keywords: dragon fruit; robotic picking; manipulator; motion characteristics; performance test

Citation: Lou, K.; Wang, Z.; Zhang, B.; Xu, Q.; Fu, W.; Gu, Y.; Liu, J. Analysis and Experimentation on the Motion Characteristics of a Dragon Fruit Picking Robot Manipulator. *Agriculture* **2024**, *14*, 2095. https://doi.org/10.3390/agriculture14112095

Received: 7 October 2024
Revised: 15 November 2024
Accepted: 18 November 2024
Published: 20 November 2024

1. Introduction

Dragon fruit (*Hylocereus*) is a tropical and subtropical fruit [1]. Rich in anthocyanins, plant albumin, and other beneficial substances, dragon fruit is highly nutritious and economically valuable [2]. With increasing market demand, global production and cultivation areas of dragon fruit continue to expand [3]. However, manual labor remains the predominant method for dragon fruit picking, resulting in high labor intensity and low operational efficiency. Hence, there is an urgent need to develop a flexible and adaptable dragon fruit picking robot to promote automation and intelligence in the dragon fruit industry.

With the rapid development of agriculture, various commercial automated machines have been developed to harvest crops such as potatoes, wheat, and maize, addressing issues such as labor shortages and low automation levels. However, research in the field of manipulator picking still faces challenging obstacles [4,5]. Xiong et al. [6] developed an autonomous strawberry picking robot capable of continuous picking by means of manual remote control of the mobile platform. Jun et al. [7] developed a tomato picking robot

that designed an end effector consisting of gripping and cutting modules. Bu et al. [8] developed an apple picking robot and analyzed two picking actions, simulated human motion and horizontal pulling and bending. Currently, researchers predominantly focus on designing and studying picking robots for strawberries, tomatoes, apples, and other fruits and vegetables [9–13]. The development of these picking robots provides valuable references for the design of robotic manipulators for dragon fruit picking. Current fruit-picking robots generally use two main methods for picking: twisting and cutting. When applying the twisting method to pick dragon fruits directly, damage is likely to occur at the base of the fruit. In contrast, most cutting-based robots are designed to pick fruits with relatively long stems that grow vertically. These robots only need to cut perpendicularly to the stem for picking. However, since the base of the dragon fruit is directly connected to its stem, picking it cannot be achieved by simply cutting the stem vertically. Instead, the cut must be made at a specific angle to avoid damaging the fruit's base while cutting the stem. Additionally, because the fruit stems are randomly distributed across various parts of the branches, the growth posture of dragon fruits is more complex than that of other fruits and vegetables. Existing fruit-picking robots cannot ensure low-damage picking of the dragon fruit's stem during the picking process. Therefore, the design of a dragon fruit picking robot must possess high flexibility and stability to handle these challenges.

In the realm of picking robots, the analysis of manipulator dynamic characteristics stands as a primary research focus. Within manipulator kinematic modeling, the Denavit–Hartenberg (D–H) method is widely applied. When using the D–H method, it is necessary to establish a local coordinate system of the system model, while the screw analysis method only needs to establish a global coordinate system and a tool coordinate system of the system model to obtain the overall model of the system. Therefore, screw theory has been successfully applied in this research field with its outstanding advantages [14]. Zhang et al. [15] designed a jujube tree pruning manipulator with five degrees of freedom and solved the kinematic equations of the jujube pruning manipulator using the D–H method. Yang et al. [16] designed a mushroom picking end effector based on negative pressure suction and calculated the position and orientation of the end effector using the D–H method. Zhang, Hu, et al. [17,18] constructed kinematic models using the D–H method, established the kinematic models of apple picking robots, and analyzed them to determine the robots' workspace. Zhang et al. [19] proposed a strawberry picking manipulator and established the kinematic model of the strawberry picking manipulator based on the D–H method. It was proved that the manipulator had no singular position within the specified range of strawberry picking points. Yang et al. [20] proposed the Product of Exponential (POE) model based on screw theory, which satisfies the requirements of parameter continuity, completeness, and minimality, avoiding the processes of standardization and orthogonalization during parameter identification. Zhang, Ge, et al. [21,22] established a kinematic model based on screw theory and derived the forward kinematic equations of the manipulator using the POE formula. Chen et al. [23] proposed an improved inverse kinematic method for a six degrees of freedom robot based on screw theory, which solved the problems of low computational efficiency and complexity of the solution of the D–H method. The analysis of dynamic equations plays a crucial role in mechanical systems research. The main methods in the dynamic modeling and solution of robotic manipulators include the Lagrangian, Newton–Euler, and Kane equations [24,25]. Wu et al. [26] utilized the Lagrangian equation to analyze the dynamic analysis of the hybrid robot mechanism. Xiao et al. [27] established a dynamic model of a heavy-duty manipulator through the Lagrangian equation to complete the research and optimization of parallel manipulators. Zhao et al. [28] developed a lightweight apple picking manipulator and established its dynamic model using the Newton–Euler equation. By analyzing the theoretical data from the dynamic model, the optimal lightweight design was selected. Farshid Asadi et al. [29] used screw theory to define the Kane equation and established a dynamic model for the manipulator. Li et al. [30] derived the nonlinear coupled dynamic equations for a four degrees of freedom tendon-driven manipulator based on Kane's equation. Andrej Cibicik

et al. [31] conducted a dynamic model and force analysis of a knuckle boom crane based on the Kane equation to determine the reaction forces of the crane, and this dynamic analysis method can be applied in a similar manipulator with any number of links. In summary, precise kinematic and dynamic models are fundamental for the research and development of picking robots. In terms of kinematics, the establishment of coordinate systems using the D–H method is relatively intricate. Additionally, singularity issues can arise when two consecutive joints of the manipulator are parallel or nearly parallel. Models based on screw theory, on the other hand, do not have singularity issues. They can provide kinematic analysis with intuitive geometric meaning and offer high solution efficiency [32,33]. In terms of dynamics, the Lagrangian and Newton–Euler equations involve numerous algebraic and differential equations during the computation process. The Kane equation uses "generalized velocities" as its fundamental parameters, allowing the derivation of dynamic equations to eliminate constraint forces and avoid the complex operations associated with the differential form of energy equations. This results in less computation, making it more suitable for computer programming and calculations [34].

To address the complex growth postures of dragon fruit, a six degrees of freedom robotic manipulator for dragon fruit picking was designed, focusing on its motion characteristics to ensure minimal damage to the stems during picking. The main contributions of this research are as follows: Firstly, a six degrees of freedom picking robot that aligns with the agronomic characteristics of dragon fruit was designed. Secondly, to reduce computational complexity, a kinematic model of the dragon fruit picking robotic manipulator was established based on screw theory, and a dynamic model was constructed using the Kane equation. Finally, a testing platform was set up to evaluate the motion characteristics of the robotic manipulator. Picking performance tests were conducted, demonstrating the reliability and stability of the robotic manipulator.

2. Dragon Fruit Picking Robot Structure Composition and Working Principles

2.1. Agronomic Characteristics of Dragon Fruit Cultivation

Dragon fruit cultivation areas are generally located on flat terrain. As shown in Figure 1a, in Hainan, dragon fruit cultivation commonly adopts a single ridge, single row, and close-planting cultivation mode to ensure uniform light exposure on both sides of the fruit. Steel cables connect the stakes in rows to support the branches, with dragon fruit stems usually attaching to the steel cables at a height of approximately 1.5 m above the ground. To minimize nutrient consumption and prevent ground-borne pests from spreading to the branches and fruit, the stems are pruned to maintain a height of at least 0.3 m above the ground. Therefore, dragon fruit generally grows within a height range of 0.3 m to 1.5 m, with row spacing between 2 and 3 m.

(**a**) (**b**)

Figure 1. Cultivation model and picking method in a dragon fruit orchard. (**a**) Cultivation mode; (**b**) Picking method.

Dragon fruit picking is a labor-intensive and timely picking task, representing a crucial component of the whole orchard management process. In Hainan, dragon fruit picking

occurs 10 to 14 times per year. Due to the need for multiple picks of dragon fruit annually, and given the short and thick fruit stems, fleshy branches, and the random distribution of fruit stems across various parts of the branches, the fruit grows on these stems with its base slightly embedded into the branch. During manual picking, it is essential to ensure a clean cut and to trim the branch at a specific angle along the base of the fruit to avoid damage to the fruit or the branch. A schematic diagram of dragon fruit picking is shown in Figure 1b. There is an urgent need for research on a dragon fruit picking robot to achieve mechanized and intelligent picking of dragon fruit [35]. The outcomes of this study are essential for promoting standardized and large-scale development of orchards.

2.2. Structure Composition

The main structure of the dragon fruit picking robot consists of a tracked chassis, a six degrees of freedom manipulator, and a vision system. The six degrees of freedom manipulator is primarily composed of a manipulator base, Joints 1–6, Links 1–5, and an end effector. The end effector mainly includes a motor, a coupling, a screw mechanism, a linkage mechanism, and a picking bucket. A schematic diagram of the dragon fruit picking robot body is shown in Figure 2.

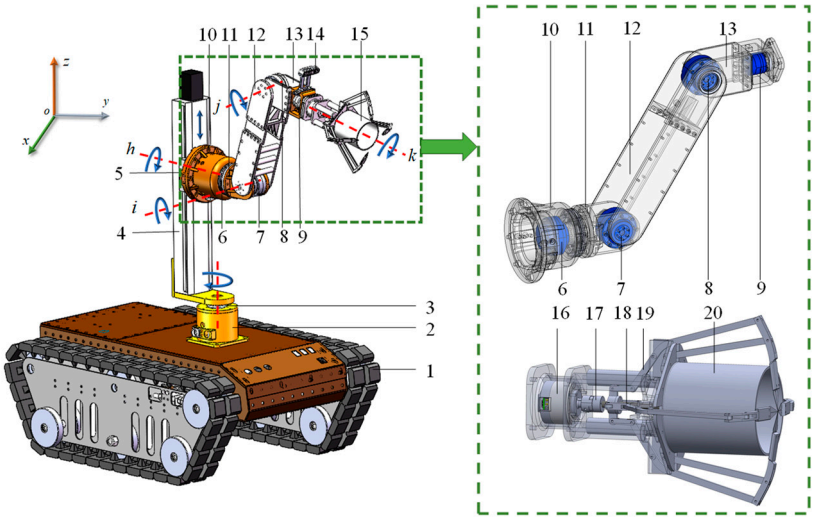

Figure 2. Dragon fruit picking robot joint motion directions and three-dimensional structure diagram. 1. Tracked chassis; 2. Manipulator base; 3. Joint 1; 4. Link 1; 5. Joint 2; 6. Joint 3; 7. Joint 4; 8. Joint 5; 9. Joint 6; 10. Link 2; 11. Link 3; 12. Link 4; 13. Link 5; 14. Vision system; 15. End effector; 16. Motor; 17. Coupling; 18. Screw mechanism; 19. Linkage mechanism; 20. Picking bucket.

2.3. Working Principles

During the operation of the dragon fruit picking robot, the vision system identifies the areas within its field of view where dragon fruits are ripe for picking. The tracked chassis is manually guided to the appropriate picking position, where the vision system recognizes and locates the ripe dragon fruits within the target range. The vision recognition system uses a depth camera to acquire depth information, calculating the three-dimensional coordinates of the center of the dragon fruit. These coordinates are relative to the base coordinate system. Based on the spatial coordinates of the pickable dragon fruits, the robotic manipulator's joints are driven to execute path planning to reach the target picking position. When the robotic manipulator reaches the target position, the end effector motor drives the movement of the screw mechanism through the coupling, controlling the linkage mechanism to perform a closing operation. The end of the linkage mechanism is equipped with a cutting blade. Once the cutting claws are fully closed, Joint 6 is actuated to rotate and cut the fruit stem. The picked dragon fruits are stored in the picking bucket. After cutting is complete, the robotic manipulator moves to the designated drop-off position, where the end effector motor drives the screw mechanism to open the linkage mechanism, placing

the dragon fruits into the fruit basket. This process achieves the mechanized picking of dragon fruits.

3. Design of the Dragon Fruit Picking Manipulator

3.1. Structural Design of the Manipulator

When manually holding scissors to pick dragon fruit, the picking operation is completed through the cooperation of each joint of the manipulator. Therefore, this study has designed a six degrees of freedom dragon fruit picking manipulator. The manipulator includes one prismatic and five rotational joints. To facilitate dragon fruit picking, Joint 1 is added to the base to achieve the picking of the whole manipulator at the same height in different directions. Joint 2 allows the manipulator to move up and down to accommodate dragon fruits at different heights. Three rotary joints (Joint 3 to Joint 5) are designed to maneuver the manipulator to the target dragon fruit position with flexibility. As dragon fruit grows directly on the stems, manual cutting involves making two cuts with scissors from the base of the fruit on both sides of the stem, resulting in a V-shaped incision. To reduce damage to the dragon fruit stems, the end effector designed in this study positions the cutting blades of the four claws at a certain angle after they are closed. This design simulates the angle used in manual cutting, avoiding damage to the fruit when the blades cut vertically at the base. Additionally, Joint 6 is added to the end effector to facilitate the rotary cutting of the stems. The structure and motion directions of the manipulator joints are shown in Figure 2. The base rotates about the z-axis, causing the motion of this joint to drive the rotation of other links and joints. The prismatic joint moves up and down along the z-axis, causing Joint 3 to Joint 6 to translate accordingly. Joint 3 to Joint 6 rotate around axes labeled as h, i, j, and k. The h-axis remains parallel to the xoy plane, the i-axis is perpendicular to the h-axis, the j-axis is parallel to the i-axis, and the k-axis is perpendicular to the j-axis. When Joint 6 rotates around the k-axis, it drives the end effector to rotate around the same k-axis simultaneously.

3.2. Dimensional Parameter Design of the Manipulator

Based on the physical characteristics of dragon fruit and its growth environment, an analysis of the required picking space was conducted. The dimensional parameters of each link and the ranges of joint motion for the dragon fruit picking robot were designed as shown in Table 1, where Link 6 refers to the end effector mentioned earlier.

Table 1. Lengths of each link and ranges of joint motion.

	Length	Joint Variables	Variable Range
Link 1	d_1	θ_1	−180–180 degree
Link 2	l_{11} (114 mm)	Δd	70–650 mm
Link 3	l_{12} (130 mm)	θ_3	−180–180 degree
Link 4	l_2 (412 mm)	θ_4	−90–90 degree
Link 5	l_{31} (168 mm)	θ_5	−144–144 degree
Link 6	l_{32} (332 mm)	θ_6	−180–180 degree

4. Kinematic and Dynamic Modeling of the Dragon Fruit Picking Manipulator

4.1. Kinematic Modeling Based on Screw Theory

Compared to the D–H method, which requires establishing local coordinate systems at each joint, using screw theory for kinematic analysis involves establishing joint axis vectors to construct the manipulator's motion model, thereby simplifying the kinematic analysis of the robot. When the joint positions are [0°, 0 mm, 0°, 0°, 0°, 0°], the dragon fruit picking manipulator is in its initial pose. A schematic of the manipulator in its initial pose is shown in Figure 3.

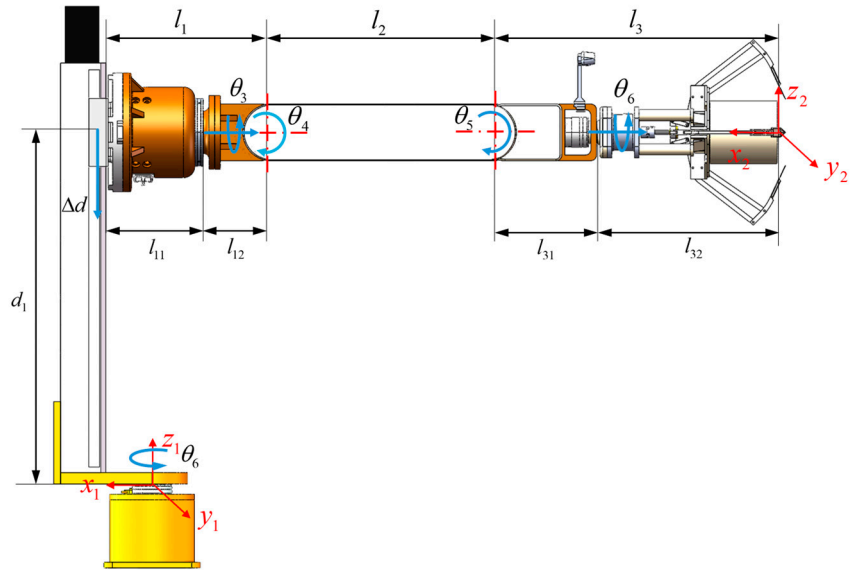

Figure 3. The initial position of the manipulator.

The motion screw coordinates ξ of a rigid body are composed of linear velocity v and angular velocity ω. Motion screws are divided into rotational joints and prismatic joints, as shown in Equation (1):

$$\xi_i = \begin{cases} \begin{bmatrix} r_i \times \omega_i \\ \omega_i \end{bmatrix} \\ \begin{bmatrix} v_j \\ 0 \end{bmatrix} \end{cases} \tag{1}$$

where ω_i is the unit vector along the motion screw axis, v_j is the unit vector in the direction of translation, and r_i is any point on the axis.

According to Chasles' theorem, the screw motion of a rigid body can be represented using the matrix exponential form of the motion screw, as shown in Equation (2):

$$e^{\hat{\xi}\theta} = \begin{cases} \begin{bmatrix} e^{\hat{\omega}\theta} & (I - e^{\hat{\omega}\theta})(\omega \times v) + \omega\omega^T v\theta \\ 0 & 1 \end{bmatrix} & \omega \neq 0 \\ \begin{bmatrix} I & v\theta \\ 0 & 1 \end{bmatrix} & \omega = 0 \end{cases} \tag{2}$$

Substituting the manipulator parameter data into Equation (2), Equations (3)–(8) are obtained.

$$e^{\hat{\xi}_1\theta_1} = \begin{bmatrix} c_1 & -s_1 & 0 & 0 \\ s_1 & c_1 & 0 & 0 \\ 0 & 0 & 1 & 0 \\ 0 & 0 & 0 & 1 \end{bmatrix} \tag{3}$$

$$e^{\hat{\xi}_2\theta_2} = \begin{bmatrix} 1 & 0 & 0 & 0 \\ 0 & 1 & 0 & 0 \\ 0 & 0 & 1 & \Delta d \\ 0 & 0 & 0 & 1 \end{bmatrix} \tag{4}$$

$$e^{\hat{\xi}_3\theta_3} = \begin{bmatrix} 1 & 0 & 0 & 0 \\ 0 & c_3 & s_3 & -d_1 s_3 \\ 0 & -s_3 & c_3 & d_1(1 - c_3) \\ 0 & 0 & 0 & 1 \end{bmatrix} \tag{5}$$

$$e^{\hat{\xi}_4\theta_4} = \begin{bmatrix} c_4 & 0 & s_4 & -l_1(1-c_4) - d_1 s_4 \\ 0 & 1 & 0 & 0 \\ -s_4 & 0 & c_4 & -l_1 s_4 + d_1(1-c_4) \\ 0 & 0 & 0 & 1 \end{bmatrix} \tag{6}$$

$$e^{\hat{\xi}_5\theta_5} = \begin{bmatrix} c_5 & 0 & s_5 & (l_1+l_2)(c_5-1) - d_1 s_5 \\ 0 & 1 & 0 & 0 \\ -s_5 & 0 & c_5 & -(l_1+l_2)s_5 + d_1(1-c_5) \\ 0 & 0 & 0 & 1 \end{bmatrix} \tag{7}$$

$$e^{\hat{\xi}_6\theta_6} = \begin{bmatrix} 1 & 0 & 0 & 0 \\ 0 & c_6 & s_6 & -d_1 s_6 \\ 0 & -s_6 & c_6 & d_1(1-c_6) \\ 0 & 0 & 0 & 1 \end{bmatrix} \tag{8}$$

where $s_i = \sin\theta_i$, $c_i = \cos\theta_i$, θ_i (i = 1, 3, 4, 5, 6) is the rotation angle of each link, and Δd is the displacement of the second link on the lifting platform.

By combining the initial position of the manipulator with the parameter data obtained from Equations (3)–(8), the POE form of the forward kinematics equation for the dragon fruit picking manipulator is derived as shown in Equation (9):

$$g_{st}(\theta) = e^{\hat{\xi}_1\theta_1} e^{\hat{\xi}_2\theta_2} \cdots e^{\hat{\xi}_6\theta_6} g_{st}(0) = \begin{bmatrix} n_x & o_x & a_x & p_x \\ n_y & o_y & a_y & p_y \\ n_z & o_z & a_z & p_z \\ 0 & 0 & 0 & 1 \end{bmatrix} \tag{9}$$

where $g_{st}(\theta)$ is the homogeneous transformation matrix of the manipulator's end effector relative to the base.

The specific expanded expressions of each term in the forward kinematics equation of the dragon fruit picking robot manipulator in Equation (9) are shown in Equation (10):

$$\begin{cases} n_x = c_1c_4c_5 + s_1s_3s_4c_5 - c_1s_4s_5 + s_1s_3c_4s_5 \\ n_y = s_1c_4c_5 - c_1s_3s_4c_5 - s_1s_4s_5 - c_1s_3c_4s_5 \\ n_z = -c_3s_{45} \\ o_x = -s_1c_3c_6 - c_1c_4s_5s_6 - s_1s_3s_4s_5s_6 - c_1s_4c_5s_6 + s_1s_3c_4c_5s_6 \\ o_y = c_1c_3c_6 - s_1c_4s_5s_6 + c_1s_3s_4s_5s_6 - s_1s_4c_5s_6 + c_1s_3c_4c_5s_6 \\ o_z = -s_3c_6 + c_3s_4s_5s_6 - c_3c_4c_5s_6 \\ a_x = -s_1c_3s_6 + c_1c_4s_5c_6 + s_1s_3s_4s_5c_6 + c_1s_4c_5c_6 - s_1s_3c_4c_5c_6 \\ a_y = c_1c_3s_6 + s_1c_4s_5c_6 - c_1s_3s_4s_5c_6 + s_1s_4c_5c_6 + c_1s_3c_4c_5c_6 \\ a_z = -s_3s_6 - c_3s_4s_5c_6 + c_3c_4c_5c_6 \\ p_x = \begin{array}{l} l_3c_1s_4s_5 - l_2c_1c_4 - l_3c_1c_4c_5 - 2d_1c_1c_4s_5 - 2d_1c_1s_4c_5 - l_1c_1 - l_2s_1s_3s_4 - l_3s_1s_3c_4s_5 - l_3s_1s_3s_4c_5 \\ -2d_1s_1s_3s_4s_5 + 2d_1c_1c_4s_5c_6 + 2d_1c_1s_4c_5c_6 + 2d_1s_1s_3c_4c_5 - 2d_1s_1s_3c_4c_5c_6 + 2d_1s_1s_3s_4s_5c_6 \end{array} \\ p_y = \begin{array}{l} l_2c_1s_3s_4 - l_2s_1c_4 - l_3s_1c_4c_5 - 2d_1s_1c_4s_5 - 2d_1s_1s_4c_5 - l_1s_1 + l_3s_1s_4s_5 + 2d_1c_1s_3s_4s_5 - 2d_1c_1s_3c_4c_5 \\ +2d_1s_1c_4s_5c_6 + 2d_1s_1s_4c_5c_6 + l_3c_1s_3c_4s_5 + l_3c_1s_3s_4c_5 + 2d_1c_1s_3c_4c_5c_6 - 2d_1c_1s_3s_4s_5c_6 \end{array} \\ p_z = l_2c_3s_4 - 2d_1c_3c_4c_5 + l_3c_3c_4s_5 + l_3c_3s_4c_5 + 2d_1c_3s_4s_5 + 2d_1c_3c_4c_5c_6 - 2d_1c_3s_4s_5c_6 + d_1 + \Delta d \end{cases} \tag{10}$$

where, $s_{ij} = \sin(\theta_i + \theta_j)$, $c_{ij} = \cos(\theta_i + \theta_j)$, ($i$= 1, 3, 4, 5, 6, j= 1, 3, 4, 5, 6).

To validate the correctness of the forward kinematics equation $g_{st}(\theta)$, the initial position of the dragon fruit picking manipulator [0°, 0 mm, 0°, 0°, 0°, 0°] was used for verification. Substituting this initial position into Equation (10) yielded results consistent with the actual initial position of the manipulator, demonstrating the correctness of the kinematic mathematical model of the manipulator based on screw theory.

4.2. Dynamical Modeling Based on Screw Theory

4.2.1. Establishment of the Kane Dynamics Equation Based on Screw Theory

The Kane equation, when dealing with the dynamics of intricate multi-degree of freedom systems, avoids the computational processes involving differentiation of second-

order differential equations. This aids in decreasing time and space complexity, enhancing efficiency, and facilitating implementation on computers. The Kane dynamic equation derived through the introduction of screw theory is shown in Equation (11):

$$\sum_{i=1}^{n} F_{\xi i}\xi'_{ij} + \sum_{i=1}^{n} F_{\xi i}{}^{*}\xi'_{ij} = \sum_{i=1}^{n}\left(\begin{pmatrix} R_i \\ M_i \end{pmatrix}\xi'_{ij}\right) + \sum_{i=1}^{n}\left(\begin{pmatrix} R^{*}_{ci} \\ M^{*}_{ci} \end{pmatrix}\xi'_{ij}\right) = 0 \tag{11}$$

where $\begin{pmatrix} R_i \\ M_i \end{pmatrix}$ and $\begin{pmatrix} R^{*}_{ci} \\ M^{*}_{ci} \end{pmatrix}$, respectively, denote the active force screw and inertia force screw acting at the center of mass of robot Link *i*. ξ'_{ij} represents the Column *j* element of the object Jacobian matrix, which corresponds to the partial velocity screw of the generalized velocity of Link *i*.

4.2.2. Calculation of Partial Velocity Screw

As shown in Figure 4, the object coordinate frames *T* for the robot links are established, where T_i (i = 1, 2, 3, 4, 5, 6) represents the object coordinate frames fixed at the center of mass of each link, and a_i (i = 1, 2, 3, 4, 5, 6) denotes the distances from the link joints to the respective centroid.

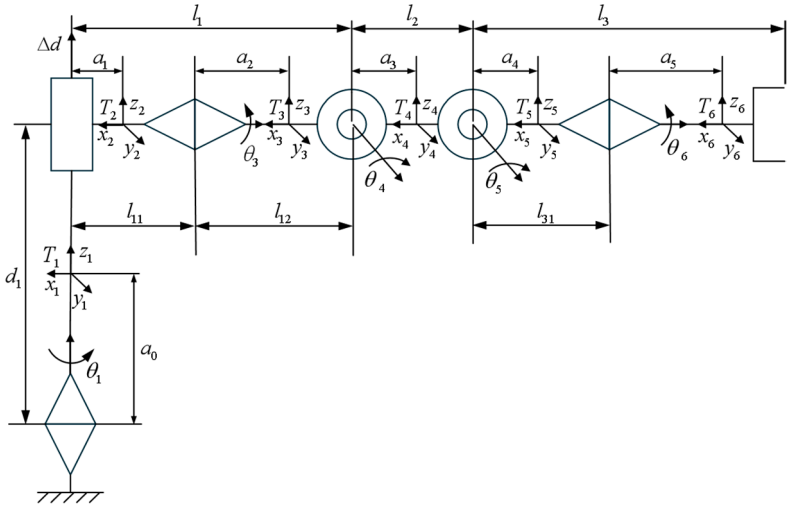

Figure 4. Schematic diagram of the manipulator.

Based on Figure 4, the instantaneous velocity screw coordinates of Joint *j* relative to the coordinate system T_i are determined as shown in Equation (12):

$$\begin{cases} \xi'_{11} = \begin{bmatrix} 0 & 0 & 1 & 0 & 0 & 0 \end{bmatrix}^T \\ \xi'_{21} = \begin{bmatrix} 0 & 0 & 1 & 0 & a_1 & 0 \end{bmatrix}^T \\ \xi'_{22} = \begin{bmatrix} 0 & 0 & 0 & 0 & 0 & 0 \end{bmatrix}^T \\ \xi'_{31} = \begin{bmatrix} 0 & s_3 & c_3 & -d_1 s_3 & (l_{11}+a_2)c_3 & -(l_{11}+a_2)s_3 \end{bmatrix}^T \\ \xi'_{32} = \begin{bmatrix} 0 & 0 & 0 & 0 & 0 & 0 \end{bmatrix}^T \\ \xi'_{33} = \begin{bmatrix} -1 & 0 & 0 & 0 & 0 & 0 \end{bmatrix}^T \\ \xi'_{41} = \begin{bmatrix} s_4 & s_3c_4 & c_3c_4 & -d_1 s_3 c_4 & d_1 s_4 + (l_1+a_3)c_3c_4 & -(l_1+a_3)s_3c_4 \end{bmatrix}^T \\ \xi'_{42} = \begin{bmatrix} 0 & 0 & 0 & 0 & 0 & 0 \end{bmatrix}^T \\ \xi'_{43} = \begin{bmatrix} -c_4 & 0 & s_4 & 0 & (l_{12}+a_3)s_4 & 0 \end{bmatrix}^T \\ \xi'_{44} = \begin{bmatrix} 0 & 1 & 0 & 0 & 0 & -a_3 \end{bmatrix}^T \end{cases} \tag{12}$$

4.2.3. Calculation of Generalized Active Forces and Generalized Inertial Forces

According to the definition of the Kane equation, the active force screw $F_{\xi i}$ of robot Link i consists of two parts: the active force principal vector R_i and the moment vector of the active force M_i about the center of mass of that link. The formula is shown in Equation (13):

$$F_{\xi i} = [R_i \; M_i]^T \tag{13}$$

The active force principal vector and the moment vector of the active force for each joint are shown in Equation (14):

$$\begin{cases} R_1 = \begin{bmatrix} 0 & 0 & -m_1 g + \tau_2 \end{bmatrix}^T \\ M_1 = \begin{bmatrix} 0 & 0 & \tau_1 \end{bmatrix}^T \\ R_2 = \begin{bmatrix} 0 & 0 & -m_2 g - \tau_2 \end{bmatrix}^T \\ M_2 = \begin{bmatrix} \tau_3 & 0 & 0 \end{bmatrix}^T \\ R_3 = \begin{bmatrix} -m_3 g s_3 & 0 & -m_3 g c_3 \end{bmatrix}^T \\ M_3 = \begin{bmatrix} -\tau_3 & \tau_4 & 0 \end{bmatrix}^T \\ R_4 = \begin{bmatrix} -m_4 g s_{34} & 0 & -m_4 g c_{34} \end{bmatrix}^T \\ M_4 = \begin{bmatrix} 0 & \tau_5 - \tau_4 & 0 \end{bmatrix}^T \\ R_5 = \begin{bmatrix} -m_5 g s_{345} & 0 & -m_5 g c_{345} \end{bmatrix}^T \\ M_5 = \begin{bmatrix} \tau_6 & -\tau_5 & 0 \end{bmatrix}^T \\ R_6 = \begin{bmatrix} -m_6 g s_{3456} & 0 & -m_6 g c_{3456} \end{bmatrix}^T \\ M_6 = \begin{bmatrix} -\tau_6 & 0 & 0 \end{bmatrix}^T \end{cases} \tag{14}$$

The generalized active forces for each joint are shown in Equation (15):

$$\begin{cases} F_1 = F_{\xi 1}^T \xi'_{11} + F_{\xi 2}^T \xi'_{21} + F_{\xi 3}^T \xi'_{31} + F_{\xi 4}^T \xi'_{41} + F_{\xi 5}^T \xi'_{51} + F_{\xi 6}^T \xi'_{61} \\ F_2 = F_{\xi 2}^T \xi'_{22} + F_{\xi 3}^T \xi'_{32} + F_{\xi 4}^T \xi'_{42} + F_{\xi 5}^T \xi'_{52} + F_{\xi 6}^T \xi'_{62} \\ F_3 = F_{\xi 3}^T \xi'_{33} + F_{\xi 4}^T \xi'_{43} + F_{\xi 5}^T \xi'_{53} + F_{\xi 6}^T \xi'_{63} \\ F_4 = F_{\xi 4}^T \xi'_{44} + F_{\xi 5}^T \xi'_{54} + F_{\xi 6}^T \xi'_{64} \\ F_5 = F_{\xi 5}^T \xi'_{55} + F_{\xi 6}^T \xi'_{65} \\ F_6 = F_{\xi 6}^T \xi'_{66} \end{cases} \tag{15}$$

The inertia force screw F_i^* of robot Link i consists of two parts: the inertia force principal vector R_{ci}^* and the moment vector of the inertia force M_{ci}^* about the center of mass of that link. The formula is shown in Equation (16):

$$F_i^* = \begin{pmatrix} R_{Ci}^* \\ M_{Ci}^* \end{pmatrix} = \begin{pmatrix} -m_i \dot{V}_{Ci}^b \\ -I_{Ci}^b \dot{\omega}_{Ti}^b - \omega_{Ti}^b \times (I_{Ci}^b \times \omega_{Ti}^b) \end{pmatrix} \tag{16}$$

where I_{Ci}^b is the inertia matrix of Joint i relative to its inertial axis, $\dot{V}_{Ci}^b$ is the centroid acceleration of Joint i, and ω_{Ti}^b and $\dot{\omega}_{Ti}^b$ are the corresponding joint angular velocity and angular acceleration, respectively.

The inertia force principal vector and the moment vector of the inertia force for each joint are shown in Equation (17):

$$\begin{cases} R_{C1}^{*} = [0\,0\,0]^{\mathrm{T}} \\ M_{C1}^{*} = [0\,0\,-I_{zz1}\ddot{\theta}_1]^{\mathrm{T}} \\ R_{C2}^{*} = [0\,0\,0]^{\mathrm{T}} \\ M_{C2}^{*} = [0\,0\,-I_{zz2}\ddot{\theta}_1]^{\mathrm{T}} \\ R_{C3}^{*} = \begin{pmatrix} 0 \\ -m_3a_2c_3^2\ddot{\theta}_1 + m_3a_2c_3\ddot{\theta}_1 + m_3a_2s_3^2\ddot{\theta}_1 \\ -m_3a_2s_3\ddot{\theta}_1 + 2m_3a_2s_3c_3\ddot{\theta}_1 \end{pmatrix} \\ M_{C3}^{*} = \begin{pmatrix} I_{xx3}\ddot{\theta}_3 + c_3s_3I_{yy3}\dot{\theta}_1^2 - c_3s_3I_{zz3}\dot{\theta}_1^2 \\ c_3(I_{xx3} + I_{yy3} - I_{zz3})\dot{\theta}_1\dot{\theta}_3 - s_3I_{yy3}\ddot{\theta}_1 \\ s_3(-I_{xx3} + I_{yy3} - I_{zz3})\dot{\theta}_1\dot{\theta}_3 - c_3I_{zz3}\ddot{\theta}_1 \end{pmatrix} \\ R_{C4}^{*} = \begin{pmatrix} -m_4a_3(\dot{\theta}_4 + s_3\dot{\theta}_1)^2 - m_4a_3(s_4\dot{\theta}_3 + c_3s_4\dot{\theta}_1)^2 + m_4c_4[a_3(\dot{\theta}_4 + s_3\dot{\theta}_1)^2 + a_3(s_4\dot{\theta}_3 + c_3s_4\dot{\theta}_1)^2 + a_2\dot{\theta}_1^2] \\ +m_4s_4[a_3(\ddot{\theta}_4 + s_3\ddot{\theta}_1 - c_3\dot{\theta}_1\dot{\theta}_3) + a_2s_3c_3\ddot{\theta}_1 + a_2c_3s_3\ddot{\theta}_1 + a_3(c_4\dot{\theta}_3 - c_3s_4\dot{\theta}_1)(s_4\dot{\theta}_3 + c_3s_4\dot{\theta}_1)] \\ -m_4a_2c_3^2\ddot{\theta}_1 + m_4a_2s_3^2\ddot{\theta}_1 \\ -m_4s_4[a_3(\dot{\theta}_4 + \dot{\theta}_1s_3)^2 + a_3(\dot{\theta}_3s_4 + c_3\dot{\theta}_1s_4)^2 + a_2\dot{\theta}_1^2] - m_4a_3(c_4\dot{\theta}_3 - c_3s_4\dot{\theta}_1)(s_4\dot{\theta}_3 + c_3s_4\dot{\theta}_1) \\ +m_4s_4[a_3(\ddot{\theta}_4 + s_3\ddot{\theta}_1 - c_3\dot{\theta}_1\dot{\theta}_3) + 2a_2s_3c_3\ddot{\theta}_1 + a_3(c_4\dot{\theta}_3 - c_3s_4\dot{\theta}_1)(s_4\dot{\theta}_3 + c_3s_4\dot{\theta}_1)] - m_4a_3(\ddot{\theta}_4 + s_3\ddot{\theta}_1 - c_3\dot{\theta}_1\dot{\theta}_3) \end{pmatrix} \\ M_{C4}^{*} = \begin{pmatrix} I_{xx4}(c_4\ddot{\theta}_3 + s_4\dot{\theta}_3\dot{\theta}_4 + c_3s_4\dot{\theta}_1\dot{\theta}_4 - c_3s_4\ddot{\theta}_1 - s_3s_4\dot{\theta}_1\dot{\theta}_3) + (I_{yy4} - I_{zz4})(s_4\dot{\theta}_3 + c_3s_4\dot{\theta}_1)(\dot{\theta}_4 + s_3\dot{\theta}_1) \\ I_{xx4}(c_4\dot{\theta}_3 - c_3s_4\dot{\theta}_1)(s_4\dot{\theta}_3 + c_3s_4\dot{\theta}_1) - I_{yy4}(\ddot{\theta}_4 + s_3\ddot{\theta}_1 - c_3\dot{\theta}_1\dot{\theta}_3) - I_{zz4}(c_4\dot{\theta}_3 - c_3s_4\dot{\theta}_1)(s_4\dot{\theta}_3 + c_3s_4\dot{\theta}_1) \\ I_{yy4}(c_4\dot{\theta}_3 - c_3s_4\dot{\theta}_1)(\dot{\theta}_4 + s_3\dot{\theta}_1) - I_{xx4}(c_4\dot{\theta}_3 - c_3s_4\dot{\theta}_1)(\dot{\theta}_4 + s_3\dot{\theta}_1) - I_{zz4}(s_4\ddot{\theta}_3 - c_4\dot{\theta}_3\dot{\theta}_4 + c_3s_4\dot{\theta}_1\dot{\theta}_4 + c_3s_4\ddot{\theta}_1 + s_3s_4\dot{\theta}_1\dot{\theta}_3) \end{pmatrix} \end{cases} \tag{17}$$

Due to the large computational complexity of dynamic modeling for a six degrees of freedom manipulator, this study presents the calculation results of the inertia force screws for Joint 1 to Joint 4 only. The inertia force screws for Joint 5 and Joint 6 of the picking manipulator can be derived analogously to the first four joints.

The generalized inertial forces for each joint are shown in Equation (18):

$$\begin{cases} F_1^{*} = F_{\xi1}^{*\,T}\xi'_{11} + F_{\xi2}^{*\,T}\xi'_{21} + F_{\xi3}^{*\,T}\xi'_{31} + F_{\xi4}^{*\,T}\xi'_{41} + F_{\xi5}^{*\,T}\xi'_{51} + F_{\xi6}^{*\,T}\xi'_{61} \\ F_2^{*} = F_{\xi2}^{*\,T}\xi'_{22} + F_{\xi3}^{*\,T}\xi'_{32} + F_{\xi4}^{*\,T}\xi'_{42} + F_{\xi5}^{*\,T}\xi'_{52} + F_{\xi6}^{*\,T}\xi'_{62} \\ F_3^{*} = F_{\xi3}^{*\,T}\xi'_{33} + F_{\xi4}^{*\,T}\xi'_{43} + F_{\xi5}^{*\,T}\xi'_{53} + F_{\xi6}^{*\,T}\xi'_{63} \\ F_4^{*} = F_{\xi4}^{*\,T}\xi'_{44} + F_{\xi5}^{*\,T}\xi'_{54} + F_{\xi6}^{*\,T}\xi'_{64} \\ F_5^{*} = F_{\xi5}^{*\,T}\xi'_{55} + F_{\xi6}^{*\,T}\xi'_{65} \\ F_6^{*} = F_{\xi6}^{*\,T}\xi'_{66} \end{cases} \tag{18}$$

Taking the link parameters from Tables 1 and 2 and substituting them into Equations (15) and (18), and then consolidating and rearranging, the expression for the standard dynamic is obtained. As shown in Equation (19), by establishing the mapping relationship between the joint angles and the required torque for driving each joint, the load capacity of the manipulator can be evaluated in different states. This ensures that the manipulator functions without overload during the stages of operation, effectively reducing design and testing costs.

$$M(\theta)\ddot{\theta} + c(\theta,\dot{\theta})\dot{\theta} + g(\theta,\dot{\theta}) = \tau \tag{19}$$

where $M(\theta)$ is the inertia matrix, $c(\theta,\dot{\theta})$ is the centrifugal and Coriolis force matrix, $g(\theta,\dot{\theta})$ is the gravity vector, and τ is the torque vector.

Table 2. Kinematic parameters of dragon fruit picking manipulator links.

	Mass/kg	**Inertia Tensor/(kg m^2)**
Link 1	$m_1 = 10$	$I_1 = \begin{bmatrix} 1.237 & -1.916\times10^{-6} & -0.235 \\ -1.916\times10^{-6} & 1.292 & 6.181\times10^{-6} \\ -0.235 & 6.181\times10^{-6} & 0.066 \end{bmatrix}$
Link 2	$m_2 = 3$	$I_2 = \begin{bmatrix} 2.054 & -2.972\times10^{-5} & -9.087\times10^{-3} \\ -2.972\times10^{-5} & 2.060 & 4.851\times10^{-4} \\ -9.087\times10^{-3} & 4.851\times10^{-4} & 1.848\times10^{-2} \end{bmatrix}$

Table 2. *Cont.*

	Mass/kg	Inertia Tensor/(kg m^2)
Link 3	$m_3 = 1.4$	$I_3 = \begin{bmatrix} 0.963 & 2.038 \times 10^{-3} & 0.198 \\ 2.038 \times 10^{-3} & 1.005 & 8.797 \times 10^{-3} \\ 0.198 & 8.797 \times 10^{-3} & 4.354 \times 10^{-2} \end{bmatrix}$
Link 4	$m_4 = 2.5$	$I_4 = \begin{bmatrix} 1.439 & -5.295 \times 10^{-3} & 0.843 \\ -5.295 \times 10^{-3} & 1.970 & -8.160 \times 10^{-3} \\ 0.843 & -8.160 \times 10^{-3} & 0.536 \end{bmatrix}$
Link 5	$m_5 = 0.7$	$I_5 = \begin{bmatrix} 0.505 & -2.283 \times 10^{-3} & 0.439 \\ -2.283 \times 10^{-3} & 0.889 & -2.648 \times 10^{-3} \\ 0.439 & -2.648 \times 10^{-3} & 0.386 \end{bmatrix}$
Link 6	$m_6 = 0.9$	$I_6 = \begin{bmatrix} 0.710 & -3.829 \times 10^{-3} & 0.782 \\ -3.829 \times 10^{-3} & 1.582 & -3.461 \times 10^{-3} \\ 0.782 & -3.461 \times 10^{-3} & 0.875 \end{bmatrix}$

5. Performance Test of the Manipulator

5.1. Establishment of Experimental Platform

An experimental platform for testing the motion characteristics of the manipulator was constructed using the prototype of the dragon fruit picking robot, as shown in Figure 5. The testing platform mainly included the prototype of the dragon fruit picking robot, a 36 V lithium-ion battery, a lower machine, an upper machine, and a depth camera. The testing platform was built using an Intel RealSense D435i depth camera to construct the visual system of a robotic manipulator, employing a dragon fruit target detection algorithm developed by the research team for target recognition [36]. The depth camera was connected to the upper computer via USB, and the ROS system processed the information from the visual system and ran the control algorithms, with the RRT-Connect algorithm used to optimize the path planning, enabling the robot to navigate efficiently and collision-free to the target position in the complex environment of the dragon fruit orchard. An STM32F407ZGT6 series microcontroller was used as the lower level controller to control the movement of the robotic manipulator to the target position for picking. The joints of the manipulator were powered by DARAN ROBOT's HCA series motors, which feature real-time feedback capabilities, allowing real-time monitoring of power, speed, and torque. Data exchange between the host computer and the lower level controller was conducted through serial communication. The host computer sent control commands to the lower level controller, which in turn provided feedback on joint speed, torque, and other parameters to the host. The host then recorded the feedback data for further analysis.

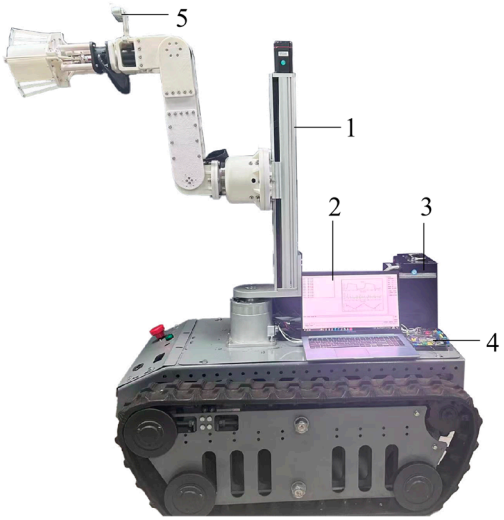

Figure 5. Schematic diagram of the manipulator. 1. Robot body; 2. Host computer; 3. 36 V lithium-ion battery; 4. Lower level controller; 5. Depth camera.

5.2. Performance Testing Plan for the Dragon Fruit Picking Manipulator

5.2.1. Workspace Simulation of the Manipulator

The workspace of the robot is constrained by factors such as the main mechanical structure and the rotation of each joint motor. A three-dimensional mathematical simulation model of the dragon fruit picking robot's manipulator was established using the MATLAB Robotics Toolbox. The workspace of the designed dragon fruit picking robot body was then simulated, and the Monte Carlo method was used to solve the robot's workspace. Based on the structural parameters of the manipulator in Table 1 and its forward kinematic model, the MATLAB Rand function was used to conduct a workspace analysis of the dragon fruit picking robot. This analysis verified whether the manipulator met the requirements for picking dragon fruit. The random values of each joint variable generated by the Rand function are shown in Equation (20).

$$\theta_i = \theta_i^{\min} + (\theta_i^{\max} - \theta_i^{\min}) \times Rand(N, 1) \tag{20}$$

where $\theta_i^{\min}$ is the minimum value of the angle or range of motion of Joint I, $\theta_i^{\max}$ is the maximum value of the angle or range of motion of Joint I, and N is the number of cycles, taking N = 10,000.

5.2.2. Performance-Testing Plan for the Manipulator

To investigate the joint motion performance of the manipulator during the dragon fruit picking operation, the manipulator's motion was controlled according to different modes and paths using the motion characteristics testing platform in a laboratory environment. It is possible to obtain key joint-related parameters such as average power consumption, rotational speed, and torque.

The motion modes of the manipulator in the experiment were categorized into trajectory planning and non-trajectory planning modes for comparative analysis. Under the same motion mode, three different picking paths are set to compare the average power consumption, rotation speed, and torque of the joints. In this study, trajectory planning involves linear motions with uniform acceleration, constant speed, and uniform deceleration. This method enables the manipulator to generate efficient trajectories under constraints of velocity and acceleration. It facilitates the coordinated motion of each joint, ensuring simultaneous arrival at the target position even when joints rotate at different angles, thereby minimizing redundant motions during operation.

In the laboratory environment, the selected positions of the dragon fruit growth and the fruit placement points are shown in Table 3. The dragon fruit picking robot has three key positions during the picking operation: the pre-picking position, the picking position, and the fruit placement position. The parameters for each position in the experiment are based on the origin of the manipulator's coordinate system, with J1 to J6 representing Joint 1 to Joint 6.

Table 3. Key positions of the manipulator during operation.

	Joint Position Parameters [J1, J2, J3, J4, J5, J6]	**Cartesian Coordinates (*x*, *y*, *z*)/m**
Pre-picking position	[0°, 0.38 m, 0°, 90°, −90°, 0°]	(−0.772, 0, 0.792)
Picking position	[0°, 0.38 m, 35°, 45°, −45°, 45°]	(−1.062, 0.192, 0.655)
Fruit placement position	[0°, 0.38 m, 0°, 15°, −105°, 45°]	(−0.670, 0, 0.0137)

Based on the design of the key working points of the manipulator, the dragon fruit picking process can be divided into three stages: picking (p1), placing the fruit (p2), and resetting (p3). The p1 stage involves moving from the pre-picking position to the picking position, the p2 stage involves moving from the picking position to the fruit placement position, and the p3 stage involves returning from the fruit placement position

to the pre-picking position. MATLAB was utilized to simulate the manipulator's dynamic model based on the Kane equation, obtaining torque information for the key joints. These simulated data were then compared with the data obtained from the motion characteristics experimental platform to verify the reliability of the dynamic model.

5.2.3. Robotic Manipulator Picking Test Plan

The picking test was conducted on 26 September 2024, at a dragon fruit orchard in Jianfeng Town, Ledong County, Hainan Province, China. The test was divided into five areas, and the dragon fruits were picked using the five-point sampling method to verify the picking performance of the dragon fruit picking robot. The picking time and picking success rate were used as evaluation indicators to assess the picking performance of the dragon fruit picking robot.

6. Results and Discussion

6.1. Workspace Simulation Analysis of the Manipulator

Based on the kinematic equations, a model for the dragon fruit picking manipulator was established, and Monte Carlo simulation was used for motion space simulation. The simulation results are shown in Figure 6, indicating that the workspace of the manipulator ranged from −1100 to 1100 mm in the *x*-direction, −1100 to 1100 mm in the *y*-direction, and −700 to 1600 mm in the *z*-direction. Since the zero point of the *z*-axis is set at the base, and considering the height of the base is 580 mm above the ground, the robotic manipulator can operate within a vertical space of 0 to 2180 mm.

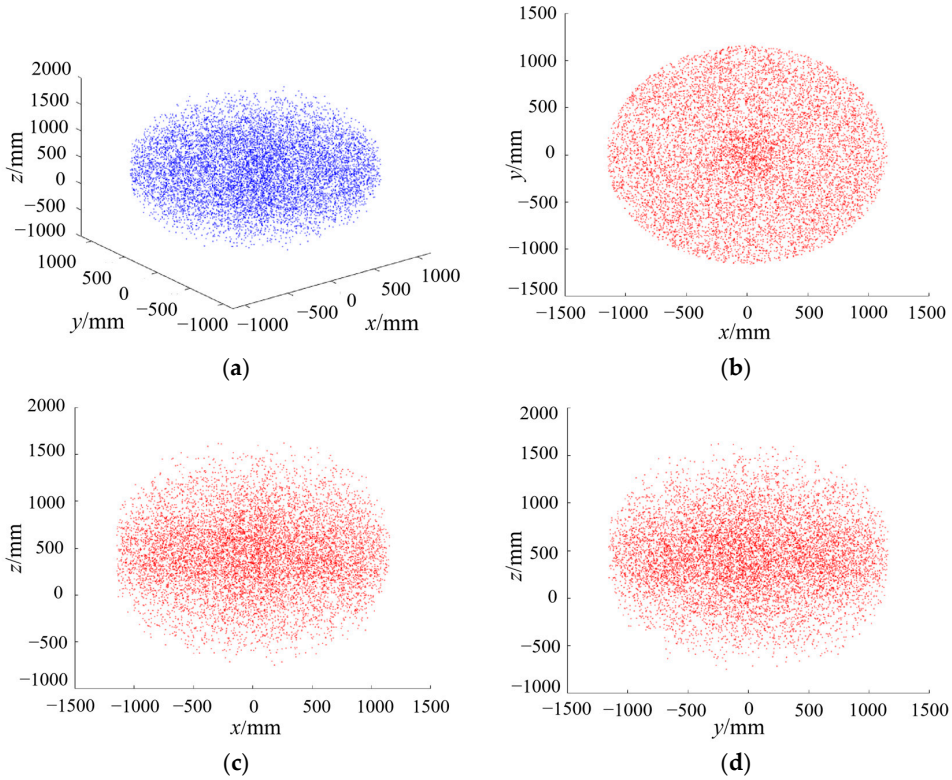

Figure 6. Dragon fruit picking robot workspace composite diagram. (**a**) Three-dimensional workspace; (**b**) *xoy* projection plane; (**c**) *xoz* projection plane; (**d**) *yoz* projection plane.

Based on the growth range of dragon fruit in the orchard, an analysis of the robotic manipulator's workspace for dragon fruit harvesting was conducted. The growth height of dragon fruit typically ranges from 0.3 m to 1.5 m, while the robotic manipulator can cover heights from ground level to 2.18 m. This allows it to effectively cover the entire growth range of the dragon fruit, ensuring the successful harvesting of both upper and

lower fruits. The typical row spacing for dragon fruit cultivation is between 2 and 3 m, allowing the robot to cover the planting area of a single row. In scenarios with greater row spacing, picking can be facilitated by adjusting the robot's movement path or deploying multiple robots. Thus, the operational range of the dragon fruit picking robot meets the spatial requirements for effective picking in agricultural settings.

6.2. Test Results and Analysis of the Manipulator Joint Speed

During the dragon fruit picking process, Joint 1 and Joint 2, which are part of the base of the manipulator, adjusted the robot's overall position and height to approximately reach the working space. Joint 3 to Joint 6 were responsible for ensuring that the end effector reached specified positions accurately and performed the picking operation. The motions of these four joints directly influenced the precision and flexibility of the end effector. Therefore, this experiment focused on analyzing the average power consumption per second of Joint 3 to Joint 6 during their operational states. As shown in Figure 7, during one pick operation, the average power consumption of the manipulator was lower under trajectory planning compared to non-trajectory planning. Taking Joint 3 as an example, the average power consumption under trajectory planning and non-trajectory planning was 4.3 W and 11.4 W, respectively, resulting in a 62.28% reduction in power consumption for the manipulator. Joint 4 and Joint 5 consumed more power compared to other joints throughout the entire picking process. Without trajectory planning, Joint 4 consumed an average of 41.4 W, and Joint 5 consumed 20.9 W. Joint 4 alone contributed to more than 65% of the total power consumption among the four joints during picking. The high power consumption of these two joints was mainly due to the need to overcome high gravitational forces in the picking process. Due to the smaller load on Joint 6, its total power consumption was the lowest among Joint 3 to Joint 6, with an average consumption of 2.5 W in both motion modes. The variation of the average power consumption was less affected during the entire picking process.

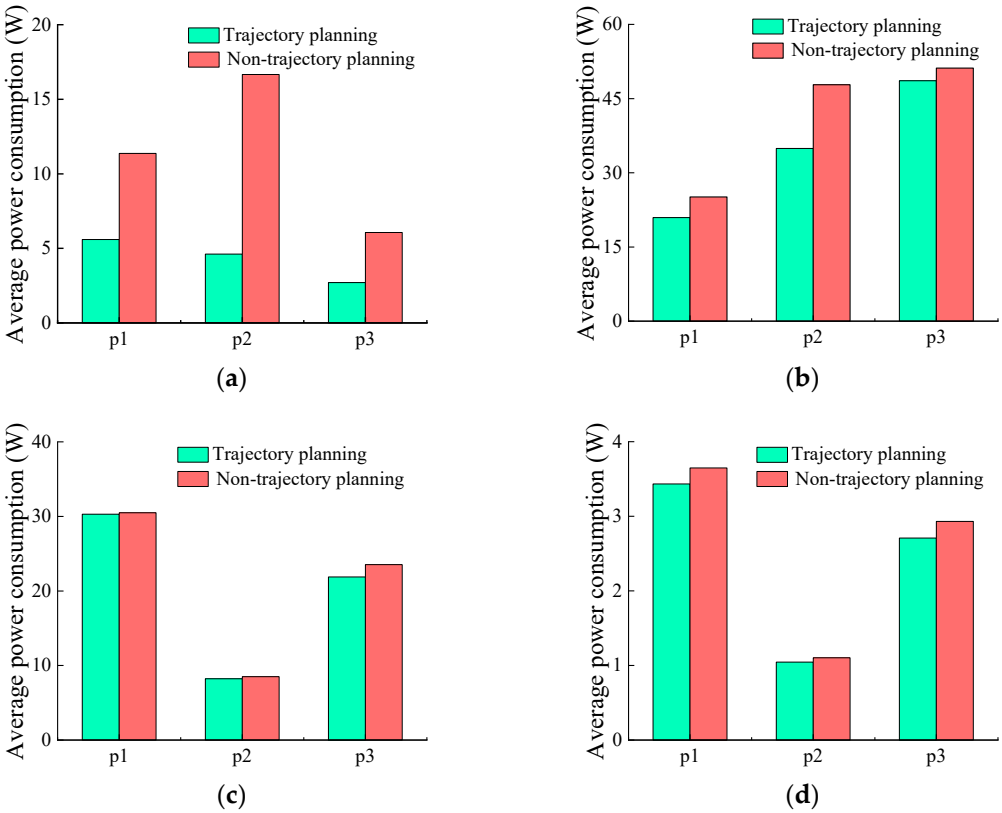

Figure 7. Joint 3 to Joint 6 average power consumption per second. (**a**) Joint 3; (**b**) Joint 4; (**c**) Joint 5; (**d**) Joint 6.

Therefore, from the perspective of reducing the average power consumption of the dragon fruit picking robot, trajectory planning reduced unnecessary energy consumption and was superior to the motion mode without trajectory planning. Among all the joints of the dragon fruit picking robot, Joint 4 had a relatively higher average power consumption compared to other joints, indicating a need for optimization in future research and design of the dragon fruit manipulator.

6.3. Test Results and Analysis of the Manipulator Joint Torque

The analysis in Section 6.2. showed that Joint 4 exhibited the highest energy consumption during the picking procedure. The motion characteristics of this joint had a significant impact on the overall performance of the manipulator. Therefore, testing was conducted on Joint 4 using the manipulator motion characteristics experimental platform to obtain the speed variation curve of the dragon fruit picking manipulator, as shown in Figure 8. From Figure 8a–c, it is observed that the operation duration of Joint 4 during the p1, p2, and p3 stages with trajectory planning was 3.3 s, 4 s, and 4.3 s, respectively. Without trajectory planning, the operation duration was 2 s, 1.6 s, and 3 s for the same stages. Under the same motion stages, the initial acceleration of Joint 4 was greater in non-trajectory planning compared to trajectory planning. Therefore, without trajectory planning, the time to reach the target position during the p1, p2, and p3 stages was faster by 1.3 s, 2.4 s, and 1.3 s, respectively, compared to trajectory planning. The joint speed directly reflected the picking speed of the dragon fruit picking manipulator, indicating that the picking speed without trajectory planning was faster than that with trajectory planning. From Figure 8d–f, it can be seen that the torque variation curve under non-trajectory planning exhibited significant fluctuations, particularly at the starting position. Due to the high acceleration during this phase and rapid velocity changes, the manipulator may have resonated, leading to a sharp increase in torque compared to other positions. Specifically, in the p1, p2, and p3 stages, the peak torques with trajectory planning were 10.14 N·m, 12.57 N·m, and 16.85 N·m, respectively. Without trajectory planning, these values increased to 12.51 N·m, 15.69 N·m, and 22.13 N·m. This indicates that trajectory planning resulted in smoother joint motion and reduced peak torque spikes on the manipulator. The adoption of trajectory planning not only enhanced the smoothness of the manipulator's motions but also improved overall operational efficiency, providing a theoretical foundation for optimization of the design of the joint motor and transmission mode of the dragon fruit picking manipulator in the future.

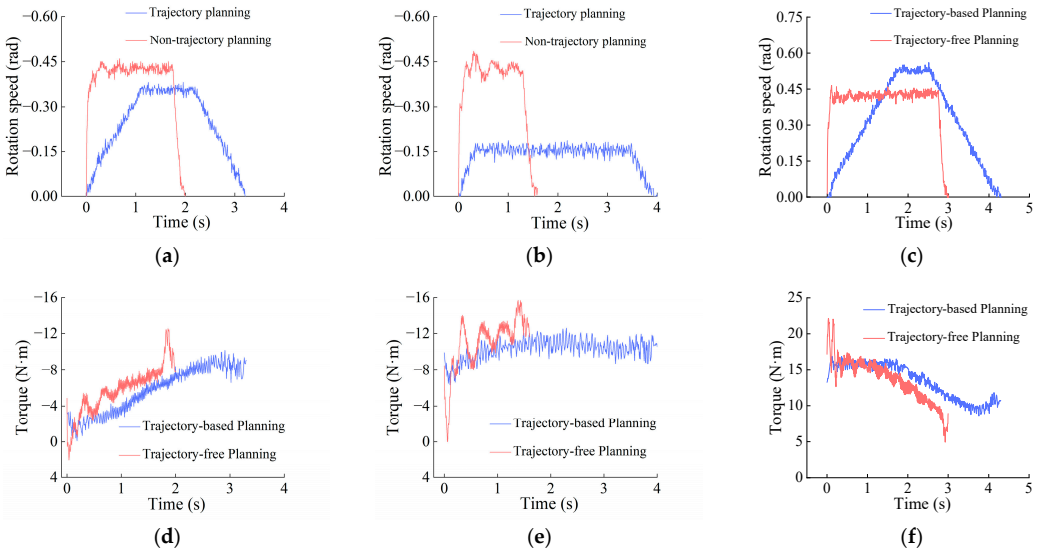

Figure 8. Joint 4 velocity and torque curves for each stage. (**a**) The p1 stage rotational speed; (**b**) The p2 stage rotational speed; (**c**) The p3 stage rotational speed; (**d**) The p1 stage torque; (**e**) The p2 stage torque; (**f**) The p3 stage torque.

6.4. Dragon Fruit Picking Manipulator Dynamics Numerical Simulation Validation

To validate the dynamics model, MATLAB R2023b was used to perform simulations under trajectory planning conditions. These simulations were compared with torque data obtained from the motion characteristics experimental platform. To ensure comprehensive data observation and recording for more accurate subsequent analysis, this experiment focused on the longest motion process, the p3 stage. It involved the simulation and testing of Joint 3 to Joint 6, as shown in Figure 9.

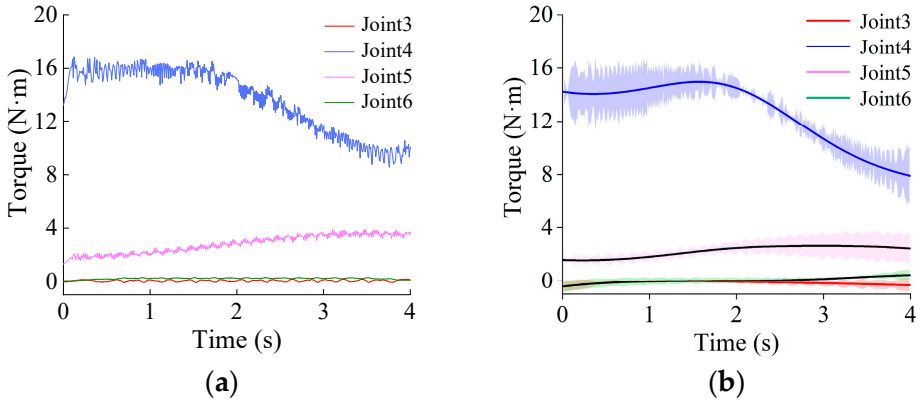

Figure 9. Torque variation curves of joints during the p3 stage. (**a**) Torque based on experimental platform; (**b**) Torque based on MATLAB simulation and its error chart.

The results showed that the variation in torques obtained from the model simulation of each joint and the torques obtained from the experimental platform, based on the motion characteristics of the manipulator in the laboratory environment, followed the same overall trend. By calculating the absolute error between the two, Joint 3 reaches its maximum absolute error of −0.48 N·m at 3.96 s, Joint 4 at −2.76 N·m at 0.36 s, Joint 5 at −1.25 N·m at 3.59 s, and Joint 6 at −0.42 N·m at 0 s. The main causes of these errors were the omission of factors such as friction in the Kane equations and external environmental influences like manipulator vibrations and electromagnetic interference, which had a certain impact on the results. Therefore, the analysis of rigid body dynamics through MATLAB simulations and experiments based on the motion characteristics experimental platform validated the correctness of the dynamics model.

6.5. Field Testing of the Dragon Fruit Picking Robot

In the field picking tests, the robot's motion mode was set to a trajectory planning mode. A total of 80 dragon fruits were picked during the tests, of which 53 were successfully picked, resulting in a success rate of 66.25%. The average picking time for a single dragon fruit was 42.4 s, and the robotic manipulator operated smoothly throughout each picking process. Approximately 75% of the dragon fruits in the test orchard were located on the outer side of the stems, while about 25% were obstructed by the stems. Among the unsuccessful picking attempts, 22.5% failed because the end effector could not reach the target position due to obstruction of the dragon fruit. Additionally, 11.25% of the failures occurred because the fruit stem was hidden, leading to difficulty in stem positioning and resulting in fruit damage during stem cutting. This experiment confirmed that the dragon fruit picking robot meets the design and operational requirements. The dragon fruit picking test process is shown in Figure 10.

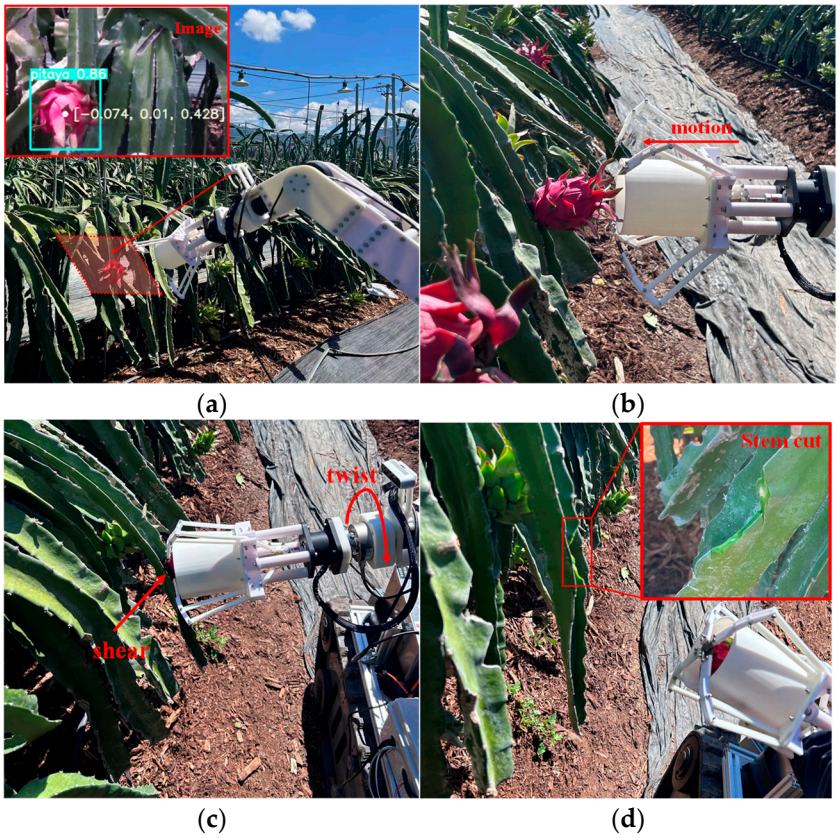

Figure 10. Field testing of dragon fruit picking robot. (**a**) Object recognition; (**b**) Moving towards the picking position; (**c**) Shearing and twisting; (**d**) Fruit picking.

7. Conclusions and Future Work

This study presented the design of a six degrees of freedom dragon fruit picking robot. A kinematic theoretical model of the manipulator was established based on screw theory. Through workspace simulation, the manipulator's working range was determined to be −1100 to 1100 mm in the x-direction, −1100 to 1100 mm in the y-direction, and −700 to 1600 mm in the z-direction, verifying its suitability for field dragon fruit picking. The dynamics model of the manipulator was derived using the Kane equation, and a prototype of the picking robot was developed. The key joints of the manipulator were evaluated based on speed, torque, and power consumption across three different motion processes, comparing trajectory planning with non-trajectory planning. The results showed that under trajectory planning, the average power consumption of the manipulator during single picking operations was significantly lower compared to non-trajectory planning. Taking Joint 3 as an example, the average power consumption under trajectory planning and non-trajectory planning was 4.3 W and 11.4 W, respectively, resulting in a 62.28% reduction in power consumption for the manipulator. Due to the influence of gravity, Joint 4 accounted for over 65% of the total energy consumption of the four joints during picking, making it a key joint for future optimization. During the picking, placing the fruit, and resetting stages, the peak torque of Joint 4 under trajectory planning was 10.14 N·m, 12.57 N·m, and 16.85 N·m, respectively. Under non-trajectory planning, the peak torque was 12.31 N·m, 15.69 N·m, and 22.13 N·m, respectively. This indicated that the manipulator operated with less impact and smoother motion under trajectory planning. During the resetting stage, MATLAB simulation and the motion characteristics experimental platform measured a maximum absolute error of −2.76 N·m for the torque generated by each joint, confirming the correctness of the dynamic equations. Through field picking experiments, it was verified that the machine's picking success rate was 66.25%, with an average picking time of 42.4 s per dragon fruit. The manipulator operated smoothly during each picking process. In

the study, the dragon fruit picking manipulator exhibited good stability, providing the theoretical foundation and technical support for intelligent dragon fruit picking.

Based on the results of the field picking experiment, the primary reason for the failure of the dragon fruit picking robot is that the dragon fruit stems obstruct the end effector from reaching the target position, and there are also difficulties in accurately positioning the fruit stem. To address these issues, future research will integrate the agricultural practices of dragon fruit cultivation to design a standardized planting model suitable for mechanical picking. By managing the pruning process, the spacing and arrangement of branches can be optimized to facilitate robot operation and reduce the likelihood of the fruit being obscured. Additionally, sensors (such as force sensors, infrared sensors, etc.) will be added to the end effector. By combining these sensors with algorithms, the robotic manipulator can more intelligently identify and locate the fruit stem, adjusting its actions based on real-time feedback to ensure low-damage picking. Path planning and trajectory optimization are essential for the stability and efficiency of the robotic manipulator during the picking process. Future research will integrate innovative trajectory planning algorithms, such as deep learning- or reinforcement learning-based path planning, to create smoother trajectories. By accounting for the spatial distribution of dragon fruit stems, the manipulator can intelligently avoid obstacles, reducing unnecessary adjustments and enhancing overall picking efficiency. Additionally, incorporating dynamic obstacle avoidance features based on real-time feedback from the vision system will allow the robot to adjust its path intelligently, minimizing collisions and further improving success rates.

Author Contributions: Conceptualization, K.L. and Z.W.; methodology, K.L. and Q.X.; software, K.L. and B.Z.; validation, K.L., Z.W., B.Z., Q.X., Y.G. and J.L.; formal analysis, K.L. and Q.X.; investigation, K.L.; resources, W.F.; data curation, K.L. and Z.W.; writing—original draft preparation, K.L. and B.Z.; writing—review and editing, K.L. and W.F.; visualization, K.L. and Y.G.; supervision, W.F. and Y.G.; project administration, W.F. and Y.G.; funding acquisition, W.F and J.L. All authors have read and agreed to the published version of the manuscript.

Funding: This research was funded by Key R&D Projects in Hainan Province (Grant No. ZDYF2022 XDNY231), the Innovation Fund for Scientific and Technological Personnel of Hainan Province (Grant No. KJRC2023D38), Key R&D Projects in Hainan Province (Grant No. ZDYF2024GXJS298) and Innovative Research Projects for Graduate Students in Hainan Province (Grant No. Qhys2023-85).

Institutional Review Board Statement: Not applicable.

Data Availability Statement: The data presented in this study are available on demand from the corresponding author at 994026@hainanu.edu.cn.

Acknowledgments: The authors would like to thank their schools and colleges, as well as the funders of the project. All support and assistance are sincerely appreciated. Additionally, we sincerely appreciate the work of the editor and the reviewers of the present paper.

Conflicts of Interest: The authors declare no conflicts of interest.

References

1. Shah, K.; Jiayi, C.; Chen, J.; Yonghua, Q. Pitaya Nutrition, Biology, and Biotechnology: A Review. *Int. J. Mol. Sci.* **2023**, *24*, 13986. [CrossRef] [PubMed]
2. Attar, H.; Gundesli, M.; Urün, I.; Kafkas, S.; Kafkas, E.; Ge, C.; Mlcek, J.; Adamkova, A. Nutritional Analysis of Red-Purple and White-Fleshed Pitaya (*Hylocereus*) Species. *Molecules* **2022**, *27*, 808. [CrossRef] [PubMed]
3. Taharuddin, N.H.; Jumaidin, R.; Mansor, M.R.; Hazrati, K.Z.; Tarique, J.; Asyraf, M.R.M.; Razman, M.R. Unlocking the Potential of Lignocellulosic Biomass Dragon Fruit (*Hylocereus polyrhizus*) in Bioplastics, Biocomposites and Various Commercial Applications. *Polymers* **2023**, *15*, 2654. [CrossRef]
4. He, Z.; Ma, L.; Wang, Y.; Wei, Y.; Ding, X.; Li, K.; Cui, Y. Double-Arm Cooperation and Implementing for Harvesting Kiwifruit. *Agriculture* **2022**, *12*, 1763. [CrossRef]
5. Kaleem, A.; Hussain, S.; Aqib Mehmood, M.; Cheema, M.J.; Saleem, S.; Farooq, U. Development Challenges of Fruit-Harvesting Robotic Arms: A Critical Review. *AgriEngineering* **2023**, *5*, 2216–2237. [CrossRef]
6. Xiong, Y.; Peng, C.; Grimstad, L.; From, P.J.; Isler, V. Development and field evaluation of a strawberry harvesting robot with a cable-driven gripper. *Comput. Electron. Agric.* **2019**, *157*, 392–402. [CrossRef]

7. Jun, J.; Kim, J.; Seol, J.; Kim, J.; Son, H. Towards an Efficient Tomato Harvesting Robot: 3D Perception, Manipulation, and End-Effector. *IEEE Access* **2021**, *9*, 17631–17640. [CrossRef]
8. Bu, L.; Chen, C.; Hu, G.; Sugirbay, A.; Sun, H.; Chen, J. Design and evaluation of a robotic apple harvester using optimized picking patterns. *Comput. Electron. Agric.* **2022**, *198*, 107092. [CrossRef]
9. Li, Z.; Yuan, X.; Wang, C. A review on structural development and recognition–localization methods for end-effector of fruit–vegetable picking robots. *Int. J. Adv. Robot. Syst.* **2022**, *19*, 802744074. [CrossRef]
10. Yu, Y.; Zhang, K.; Liu, H.; Yang, L.; Zhang, D. Real-Time Visual Localization of the Picking Points for a Ridge-Planting Strawberry Harvesting Robot. *IEEE Access* **2020**, *8*, 116556–116568. [CrossRef]
11. Gao, J.; Zhang, F.; Zhang, J.; Guo, H.; Gao, J. Picking patterns evaluation for cherry tomato robotic harvesting end-effector design. *Biosyst. Eng.* **2024**, *239*, 1–12. [CrossRef]
12. Ji, W.; He, G.; Xu, B.; Zhang, H.; Yu, X. A New Picking Pattern of a Flexible Three-Fingered End-Effector for Apple Harvesting Robot. *Agriculture* **2024**, *14*, 102. [CrossRef]
13. Xu, H.; Yu, G.; Niu, C.; Zhao, X.; Wang, Y.; Chen, Y. Design and Experiment of an Underactuated Broccoli-Picking Manipulator. *Agriculture* **2023**, *13*, 848. [CrossRef]
14. Gallardo-Alvarado, J.; Garcia-Murillo, M.A.; Alcaraz-Caracheo, L.A.; Torres, F.J.; Sandoval-Castro, X.Y. Forward Kinematics and Singularity Analyses of an Uncoupled Parallel Manipulator by Algebraic Screw Theory. *IEEE Access* **2022**, *10*, 4513–4522. [CrossRef]
15. Zhang, B.; Chen, X.; Zhang, H.; Shen, C.; Fu, W. Design and Performance Test of a Jujube Pruning Manipulator. *Agriculture* **2022**, *12*, 552. [CrossRef]
16. Yang, S.; Ji, J.; Cai, H.; Chen, H. Modeling and Force Analysis of a Harvesting Robot for Button Mushrooms. *IEEE Access* **2022**, *10*, 78519–78526. [CrossRef]
17. Zhang, K.; Lammers, K.; Chu, P.; Li, Z.; Lu, R. System design and control of an apple harvesting robot. *Mechatronics* **2021**, *79*, 102644. [CrossRef]
18. Hu, G.; Chen, C.; Chen, J.; Sun, L.; Sugirbay, A.; Chen, Y.; Jin, H.; Zhang, S.; Bu, L. Simplified 4-DOF manipulator for rapid robotic apple harvesting. *Comput. Electron. Agric.* **2022**, *199*, 107177. [CrossRef]
19. Zhang, Y.; Zhang, K.; Yang, L.; Zhang, D.; Cui, T.; Yu, Y.; Liu, H. Design and simulation experiment of ridge planting strawberry picking manipulator. *Comput. Electron. Agric.* **2023**, *208*, 107690. [CrossRef]
20. Yang, X.; Wu, L.; Li, J.; Chen, K. A minimal kinematic model for serial robot calibration using POE formula. *Robot. Comput.-Integr. Manuf.* **2014**, *30*, 326–334. [CrossRef]
21. Ge, D. Kinematics modeling of redundant manipulator based on screw theory and Newton-Raphson method. *J. Phys. Conf. Ser.* **2022**, *2246*, 12068. [CrossRef]
22. Zhang, Y.; Xiao, A.; Wu, A.; Yue, H.; Du, X. Parameter Calibration on Replacement Manipulator for UHV Valve-Side Bushing Based on Spinor Theory. *Math. Probl. Eng.* **2021**, *2021*, 3281606. [CrossRef]
23. Chen, Q.; Zhu, S.; Zhang, X. Improved Inverse Kinematics Algorithm Using Screw Theory for a Six-DOF Robot Manipulator. *Int. J. Adv. Robot. Syst.* **2015**, *12*, 140. [CrossRef]
24. Zhao, J.; Sun, H.; Li, H.; Zhao, D. Screw Dynamics of a Multibody System by a Schoenflies Manipulator. *Appl. Sci.* **2023**, *13*, 9732. [CrossRef]
25. Talaeizadeh, A.; Forootan, M.; Zabihi, M.; Nejat Pishkenari, H. Comparison of Kane's and Lagrange's Methods in Analysis of Constrained Dynamical Systems. *Robotica* **2020**, *38*, 2138–2150. [CrossRef]
26. Wu, J.; Zhang, B.; Wang, L.; Yu, G. An iterative learning method for realizing accurate dynamic feedforward control of an industrial hybrid robot. *Sci. China Technol. Sci.* **2021**, *64*, 1177–1188. [CrossRef]
27. Xiao, Y.; Sun, J.; Chen, T.; Fan, X. Analysis and optimization for the counter-balancing method of heavy-load palletizing manipulators. In Proceedings of the 2013 International Conference on Advanced Mechatronic Systems, Luoyang, China, 25–27 September 2013.
28. Zhao, X.; Cao, G.; Zhang, P.; Ma, Z.; Zhao, L.; Chen, J. Dynamic Analysis and Lightweight Design of 3-DOF Apple Picking Manipulator. *Trans. Chin. Soc. Agric. Mach.* **2023**, *54*, 88–98. [CrossRef]
29. Asadi, F.; Sadati, S.H. Full Dynamic Modeling of the General Stewart Platform Manipulator via Kane's Method. *Iran. J. Sci. Technol. Trans. Mech. Eng.* **2018**, *42*, 161–168. [CrossRef]
30. Li, K.; Zhang, Y.; Hu, Q. Dynamic modelling and control of a Tendon-Actuated Lightweight Space Manipulator. *Aerosp. Sci. Technol.* **2019**, *84*, 1150–1163. [CrossRef]
31. Cibicik, A.; Egeland, O. Dynamic modelling and force analysis of a knuckle boom crane using screw theory. *Mech. Mach. Theory* **2019**, *133*, 179–194. [CrossRef]
32. Zhao, G.; Jiang, D.; Liu, X.; Tong, X.; Sun, Y.; Tao, B.; Kong, J.; Yun, J.; Liu, Y.; Fang, Z. A Tandem Robotic Arm Inverse Kinematic Solution Based on an Improved Particle Swarm Algorithm. *Front. Bioeng. Biotechnol.* **2022**, *10*, 832829. [CrossRef] [PubMed]
33. Sun, P.; Li, Y.; Wang, Z.; Chen, K.; Chen, B.; Zeng, X.; Zhao, J.; Yue, Y. Inverse displacement analysis of a novel hybrid humanoid robotic arm. *Mech. Mach. Theory* **2020**, *147*, 103743. [CrossRef]
34. Huang, Q.; Zhou, J.; Chen, X.; Yao, Y.; Chen, Y.; Chen, W.; Chen, R.; Lv, Z. Modeling and Control of a Two-Axis Stabilized Gimbal Based on Kane Method. *Sensors* **2024**, *24*, 3615. [CrossRef] [PubMed]

35. Zhang, J.; Kang, N.; Qu, Q.; Zhou, L.; Zhang, H. Automatic fruit picking technology: A comprehensive review of research advances. *Artif. Intell. Rev.* **2024**, *57*, 54. [CrossRef]
36. Zhang, B.; Wang, R.; Zhang, H.; Yin, C.; Xia, Y.; Fu, M.; Fu, W. Dragon fruit detection in natural orchard environment by integrating lightweight network and attention mechanism. *Front. Plant Sci.* **2022**, *13*, 1040923. [CrossRef]